On the Evolution and Structure of a Radiation Fog Event in Nanjing

LIU Duanyang (刘端阳), YANG Jun (杨 军), NIU Shengjie*(牛生杰), and LI Zihua (李子华)

Key Laboratory for Atmospheric Physics and Atmospheric Environment,

Nanjing University of Information Science & Technology, Nanjing 210044

ABSTRACT

An extremely dense radiation fog event during 10–11 December 2007 was studied to understand its macro-/micro-physics in relation to dynamic and thermodynamic structures of the boundary layer, as well as its structural evolution in conjunction with the air-surface exchange of heat and water vapor. The findings are as follows. The extreme radiation fog process was divisible into formation, development, mature, and dissipation phases, depending on microstructure and visibility. This fog event was marked by rapid evolution that occurred after sunrise, when enhanced surface evaporation and cold air intrusion led to a three order of magnitude increase in liquid water content (LWC) in just 20 minutes. The maximum droplet diameter (MDD) increased four-fold during the same period. The fog structure was two-layered, with the top of both the surface-layer and upper-layer components characterized by strong temperature and humidity inversions, and low-level jets existed in the boundary layer above each fog layer. Turbulence intensity, turbulent kinetic energy, and friction velocity differed remarkably from phase to phase: these features increased gradually before the fog formation and decreased during the development phase; during the mature and dissipation phases these characteristics increased and then decreased again. In the development and mature stages, the mean kinetic energy of the lower-level winds decreased pronouncedly, both in the horizontal and vertical directions.

Key words: Nanjing, dense fog, dynamic and thermodynamic structures, intrusion, turbulence

1. Introduction

Radiation fog results from turbulent transfers of momentum, heat, and water vapor in conjunction with surface radiative cooling and microphysical processes in the boundary layer. Such fogs easily occur amid weather patterns favorable for temperature inversion and their existence is intimately tied to the exchange of vapor and heat between air and surface. Since the early 20th century (Taylor, 1917) intensive studies have been undertaken concerning the physical mechanism for fog formation by means of field observations (e.g., Huang et al., 1992; Fuzzi et al., 1992; Huang et al., 1998a, b; Li et al., 1999; Ahn et al., 2003; Zhang et al., 2005; Gultepe et al., 2007; Pu et al., 2008a, b; Niu et al., 2010) and numerical simulations (e.g., Bott et al., 1990; Duynkerke, 1991; Zhang and Li, 1993; Bergot and Guedalia, 1994; Yin and Xu, 1994; Cao et al., 1998; Zeng and Huang, 1998; Huang et al., 2000; Nakanishi, 2000; Nishikawa et al., 2004; Gao et al., 2007; Zhou and Ferrier, 2008).

Many observational studies show that the development of radiation fog depends mainly on the balance between radiative cooling and turbulence. Also, soil thermal flux in association with surface heat transfer and radiative cooling plays a prominent role in the formation and development stages. As noted in Zhang et al. (2005), turbulent activities excited by increased lower-level wind shear contribute to radiation fog formation.

Li et al. (1999) documented a radiation fog event for its explosive intensification and deepening, assuming the multi-layered temperature inversions to be an important factor favoring this explosiveness and the

---

*Corresponding author: NIU Shengjie, niusj@nuist.edu.cn

turbulent mixing-induced vertical transport of heat, momentum, and moisture. In particular, the authors considered that the downward transfer of water vapor from the upper-level high-moisture zone to be of non-trivial importance to the rapid intensification process.

Nakanishi (2000) carried out a numerical experiment on radiation fog to investigate and validate the fog structure and the mechanisms behind its formation. They indicated that before formation, the atmospheric stratification was stable, with an inversion layer immediately above the surface; during development the stratification became unstable, leading to the occurrence of a mixed layer. It is noted that the turbulent structure varies in the formation, development, and dissipation phases of radiation fog.

Through a theoretical study, Zhou and Ferrier (2008) concluded that the fog boundary layer (FBL) was marked by thinner layer of weak turbulence and intense cooling. With increased turbulence or a decreased cooling rate, the FBL would develop directly from the surface; the deeper the fog, the greater degree of turbulence could be inside. If the turbulence were below a threshold value, the fog would be maintained. When the turbulence level is above the threshold value or extends higher than the depth of the FBL, the balance will not be sustained, resulting in a gradual dispersal of fog.

These earlier studies investigated the dynamic and thermodynamic structures of radiation fog from its formation to dissipation based on *in situ* observations and numerical models by conducting analyses of the role of turbulence and radiation in radiation fog's life cycle from a range of perspectives. Many observational projects have not considered every aspect of the problem, such as fog's macro-/micro-structure, or the variation in turbulence and radiation could not be revealed at different stages. A radiation fog's physics involves several phases (formation, development, mature, and dissipation), in which turbulence and radiation change from one phase to the next. Factors affecting fog are many, including air-surface exchanges of heat and water vapor in addition to dynamic and thermal factors.

On the campus of Nanjing University of Information Science & Technology (NUIST), winter fog observations were made each year in 2006–2008, including the structure of the FBL, microphysical parameters, turbulence, radiation, and thermal equilibrium components. These field observations were undertaken successively for the whole fog process in an effort to reveal its formation/dissipation physics as well as the boundary-layer structure and macro-/micro-physical characteristics, and to gain insight into the triggering and maintenance mechanisms of radiation fog and extremely dense fog. The event during 10–11 December 2007 was studied and is presented here. Intensive analysis was performed on the boundary-layer dynamic and thermodynamic structures in various phases of fog evolution, with particular focus on the factors responsible for the fog's explosive development. We find that the extreme radiation fog event showed great differences in microstructure and visibility from phase to phase, that the turbulence was structured in a greatly different manner from phase to phase, and that the intense radiation fog was marked by explosive reinforcement and dual-level structure.

Following the introduction, section 2 briefly describes the observations, instruments, and data processing. Section 3 concerns the fog formation and dissipation in conjunction with its microstructure. Section 4 investigates the fog-related dynamic and thermodynamic structures in the boundary layer. Section 5 examines the disturbances of the boundary-layer wind field. Section 6 discusses the variations in radiation flux and air-surface exchanges of heat and water vapor, with a summary presented in section 7.

2. Observations, instruments, and data processing

The observational site was the meteorological observation station of the NUIST (32°12′N, 118°42′E, 25 m above the sea level), located on flat ground with no high buildings and trees within 200 meters. The instruments included a fog measuring device (FMD; FM-100), a visibility meter, an automatic weather station, an acoustic Doppler radar, a tether-sonde system, and an open path eddy covariance system that was installed over a grassy plot (see Table 1).

The fog monitor, visibility meter, and automatic weather station were functioning during the entire observation period (Liu et al., 2010). The acoustic radar detected the 3D vertical winds in the boundary layer, with an effective probed height reaching ∼500 m above ground and a wind profiler that provided a complete set of wind directions/velocities at 15-min intervals. The tether-sonde system observed the vertical distributions of temperature, pressure, humidity, and wind in the atmosphere, usually at 3-h intervals (and once per hour when fog appeared). The open path eddy covariance measuring system (Siebert and Teichmann, 2000) consisted of a CR5000 data collector, CSAT3 ultrasonic anemometer, and LI7500 CO_2/H_2O analyzer. The CR5000 controlled data measurement, operation, and storage. The CAST3 was responsible for 3D wind velocity and ultrasonic virtual temperature. The LI7500 measured CO_2 and water vapor fluxes. The system calculated flux on-line, storing the data

Table 1. List of instruments used during the project.

Instruments	Measurement	Resolution time	Precision
Tether-sonde systems (DigiCORA III, Vaisala, Finland)	T, pressure, RH, wind	1–3 s	T: 0.1°C; pressure: 0.1 hPa; RH: 0.1%; wind: 0.1 m s^{-1};
Visibility meter (ZQZ-DN, Jiangsu Province Radio Science Institute, China)	visibility	15 s	10%, <1000 m; 20%, >1000 m;
Fog Measuring Device (FM-100,DMT,USA)	fog droplet spectrum	1 s	Range 2–50 μm;
Ultrasonic anemometer (CSAT3, Campbell, USA)	3D wind velocity, ultrasonic virtual temperature	0.1 s	u,v: 1 mm s^{-1}; w: 0.5 mm s^{-1}; UVT: 0.002°C;
Temperature and RH Probe (HMP45C, Campbell, USA)	T, RH	15 s	T: 0.2°C–0.5°C $\pm$2% RH (0 to 90% RH) $\pm$3% RH (90% to 100% RH)
Heat flux transducer (HFP01-L, Campbell, USA)	heat flux	< 18 s	within -15% to $+5$% in most common soils
Water content reflectometers (S616-L, Campbell, USA)	soil water content		0.05%
Radiation (CNR-1, Kipp & Zonen, Netherlands)	incoming and outgoing short-wave and long-wave	< 18 s	
CO$_2$/H$_2$O analyzer (Li7500, LiCor Inc, USA)	CO$_2$ and water vapor fluxes	0.1 s	
Automatic weather station (EnviroStation$^{\mathrm{TM}}$, ICT, Australia)	T, pressure, RH, wind	1 s–1 h	1%–3%;
Acoustic radar(MFAS, Scintec Corporation German)	3D vertical winds	15 min	effective height: 500 m in fog

and time sequence in the computer. In dealing with the characteristics of the boundary layer during a fog event, a scheme of 1-min averaging was utilized for the 3D winds, ultrasonic virtual temperature, vapor, and CO$_2$ flux measurements. The other transducers included HMP45C sondes for temperature and relative humidity, a HFP01 heat flux plate (i.e., heat flux transducer), a soil temperature sensor, and a water content transducer in conjunction with a set of instruments for net radiation (Kipp & Zonen CNR-1) that was comprised of two solar radiometers and two ground radiometers for measuring the corresponding short- and long-wave radiation, respectively, with the data averaged over 1 min for storage. The LI7500C0$_2$, vapor analyzer, ultrasonic CSAT3, and HMP45C (CNR-1) had their sondes located at roughly 3 m (1.5 m for the CNR-1) above ground, while the thermal flux plate, soil temperature, and moisture content transducers were placed horizontally at 10-cm depth under the surface. The open path eddy covariance system had its data collected synchronously with the other instruments. To guarantee data quality, the following turbulence data were removed, (Zhang et al., 2004) including (1) winds with an angle of greater than $\pm7°$ with the horizontal plane; (2) winds having a mean velocity less than 0.2 m s^{-1}; (3) friction velocities less than 0.02 m s^{-1}; (4) sensible heat flux H_S less than 2 W m^{-2}; (5) other data for which it was impossible to

guarantee the homogeneity of turbulence data.

3. Fog formation and dissipation in conjunction with its microstructure

On the weather charts for 10 December 2007 there was a high to the west of Baikal. North China was covered with a homogeneous pressure regime, with a inverted trough stretching from Fujian and crossing Zhejiang to Jiangsu when it was drizzling (see Fig. 1) at the observational site until 1000 LST. This was followed by overcast conditions until 2000 LST. After 2000 LST, the homogeneous pressure area moved southward and the inverted trough crossed into the ocean area, which formed a maritime low-pressure center. This led to conditions at the observation site that were controlled by a clear sky high pressure zone. In such fair weather, there is radiative cooling in the near-surface layer, and the visibility began to drop to less than 1000 m at 2230 LST on 10 December when the fog occurred. As temperatures dropped further, the fog became thicker and thicker, leading to a dense fog (horizontal visibility L <500 m) around midnight according to the China Meteorological Administration (CMA) definition (2003). Visibility declined to 200 m at 0130 LST on 11 December, varying thereafter between 100 and 300 m until 0730 LST (35 min after sun-
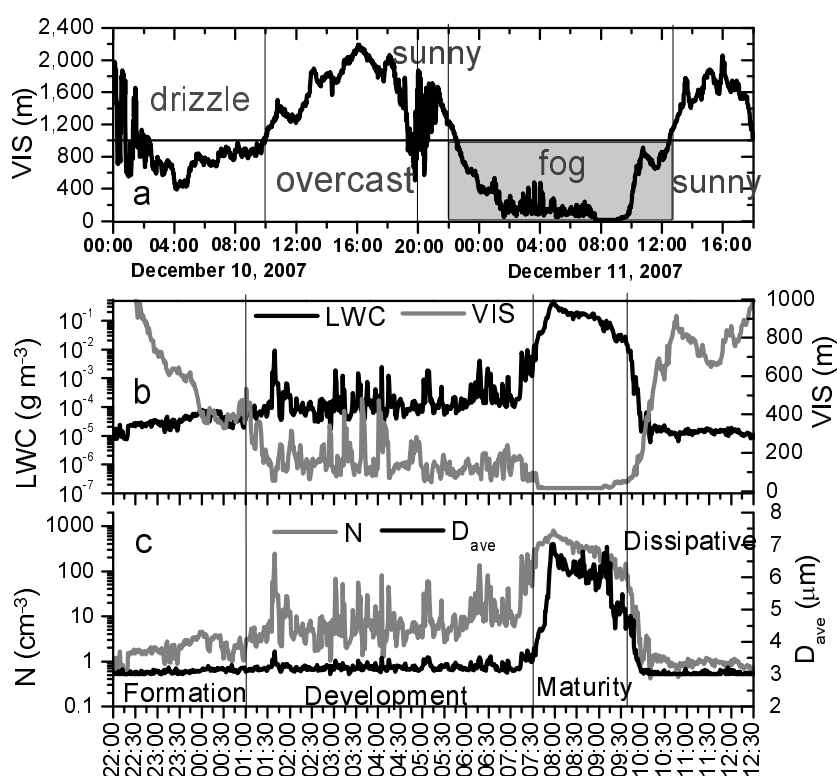
Fig. 1. Time-dependent visibility and fog microphysical parameters from formation until dispersal during 10–11 December 2007. The period plotted in panels (b) and (c) is related to the shaded period in panel (a). LWC=the liquid water content of fog, Vis = visibility, N = the number density of fog droplets, D_{ave} = the averaged diameter over droplets.

rise), when the surface fog intensified explosively to an extremely dense fog ($L < 50$ m, according to the CMA definition), with visibility dropping to less than 15 m. The extremely dense fog lasted for more than 2 h. As solar radiation became stronger, the near-surface-layer temperature rose gradually. At 0940 LST on 11 December, the fog started to weaken, permitting visibility to increase. The event dispersed at 1230 LST.

Figure 1 shows changes in microphysical parameters during the fog process. The visibility was negatively correlated with concentration (N), liquid water content (LWC), and average diameter (D_{ave}); when the visibility dropped to 200 m from 1000 m, the LWC increased to 0.0001 g m^{-3}. While the visibility fluctuated around 200 m, the LWC varied between 0.0001 and 0.005 g m^{-3} and N changed correspondingly between 7 and 100 cm^{-3}. Finally, the visibility was reduced to somewhat better than 100 m, and then LWC exceeded 0.005 g m^{-3} and N was above 100 cm^{-3} (Table 2 and Fig. 2). Based on the variations in visibility and microphysical parameters, the fog event was separated into its formation, development, mature, and dissipation phases.

Table 2. Interrelationship of visibility to LWC and N.

Visibility (m)	LWC (g m^{-3})	N (cm^{-3})
200–1000	<0.0001	<7
~200	0.0001–0.005	7–100
<100	>0.005	>100

Table 3 shows the primary physical characteristics of the fog in each of the four phases. Prior to fog formation, the above listed microphysical parameters were very small. When the fog was generated, the visibility descended, and N and LWC increased slightly compared their pre-fog values, except that N was still lower than 5 cm^{-3}, LWC averaged 0.000038 g m^{-3}, and the maximum droplet diameter (MDD) was still less than 6 μm on average. During the development phase, N and LWC increased by one order of magnitude, arriving at levels of 10 cm^{-3} and 10^{-4} g m^{-3}, respectively, and with the MDD broadening to 7.5 μm. During 0720–0740 LST (sunrise was at 0655 LST) on 11 December, the fog's denseness was greatly enhanced and the microphysical parameters increased sharply, with visibility dropping to 15 m, signaling that the fog

Table 3. Microphysical properties of the Nanjing dense fog in its different phases (denoted by local standard time) on 10–11 December 2007.

Phase		Visibility (m)	N (cm^{-3})	LWC (g m^{-3})	$D_{\max}$ (μm)	D_{ave} (μm)
pre-fog	mean	1254	1.0	0.000016	4.82	3.03
	max	2190	1.9	0.000026	6.00	3.24
	min	394	0.5	0.000007	4.00	3.00
formation	mean	565	2.3	0.000038	5.91	3.10
(2231–0130)	max	984	4.6	0.000081	6.00	3.28
	min	328	0.9	0.000013	4.00	3.00
development	mean	163	15.2	0.000396	7.40	3.22
(0131–0730)	max	533	248.1	0.009291	16.00	3.73
	min	48	1.0	0.000015	4.00	3.00
mature	mean	24	329.8	0.131	30.56	5.73
(0731–0940)	max	95	798.6	0.472	38.00	7.03
	min	15	48.2	0.00421	14.00	3.54
dissipation	mean	659	2.5	0.000243	6.17	3.12
(0941–1230)	max	979	42.0	0.009171	26.00	4.81
	min	62	0.4	0.000006	4.00	3.00
post-fog	mean	1193	1.7	0.0000234	4.4	3.01
	max	2057	8.3	0.000121	6.00	3.22
	min	376	0.1	0.000001	4.00	3.00
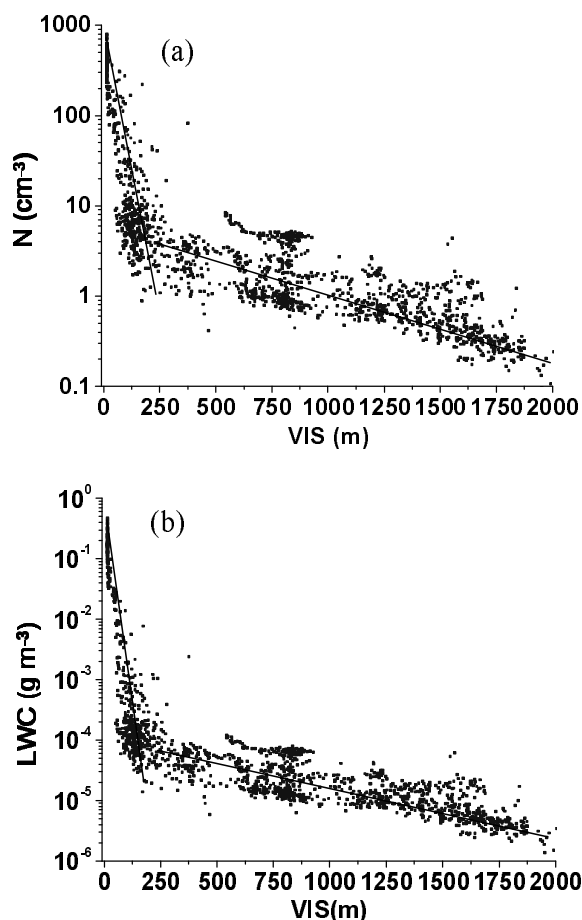
Fig. 2. Scatter diagram of visibility relative to the number density of (a) droplets (N) and (b) LWC in during fog occurrence.

had arrived at its mature stage. In this phase, the mean LWC was 0.13 g m^{-3}, with a maximum value of 0.47 g m^{-3}, and the mean MDD reached 30 μm, with a peak value of 38 μm, implying that fog droplet growth increased via condensation and coalescence in this stage. In the dissipation phase the visibility increased but all the microphysical parameters decreased rapidly in magnitude, with N and LWC comparable to those in the formation stage.

4. Macro-scale dynamic and thermodynamic structure in the boundary layer during the fog process

The fog's micro-scale evolution was under the influence of the macro-scale dynamic and thermodynamic structures in the boundary layer and the fluctuations of the low-level winds. In addition, the fog's formation and development were impacted by the air-surface exchange of heat and vapor.

4.1 *Vertical structure of temperature and humidity*

Figure 3 depicts the vertical profiles of temperature, humidity, and winds for several observation times after the fog's explosive development. The fog was dual-layered, and the temperature and humidity inversion also had double layers. The bottom-level fog had its top at 100–125 m altitude and the upper-layer fog was first present at the 300–400 m level (0840 LST) and then descended to 270–370 m (0920 LST). The lower-level temperature of the surface fog was dis-
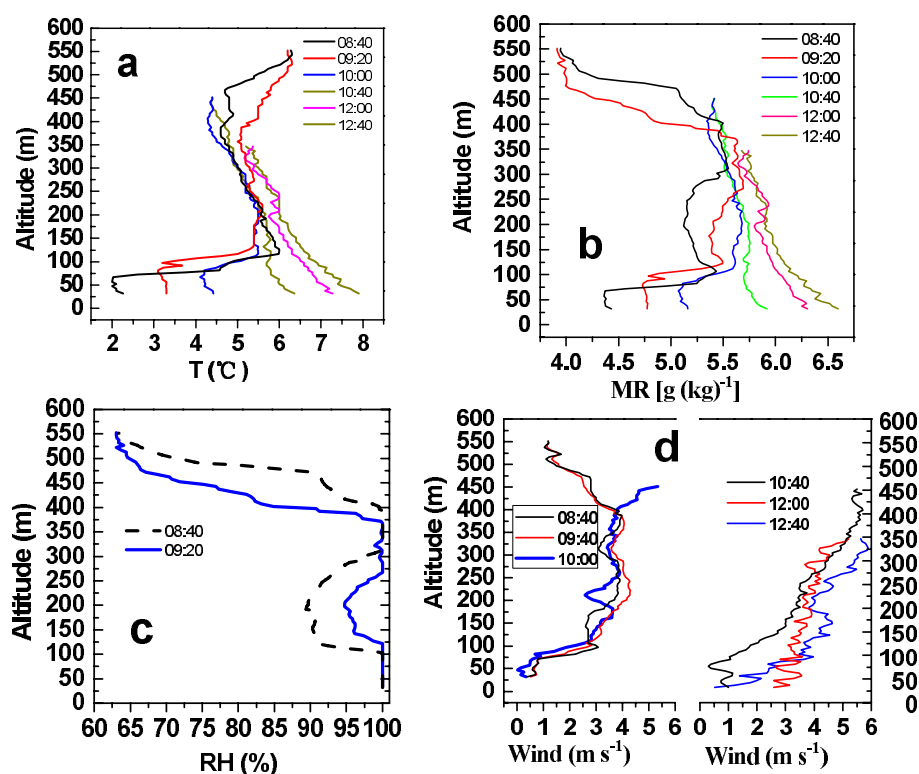
Fig. 3. Profiles of (a) temperature (T; °C), (b) mixing ratio (MR; g kg^{-1}), (c) relative humidity (RH; %), and (d) wind (m s^{-1}) in the four phases of extremely dense fog on 11 December 2007.

tributed mainly moist adiabatically, with the fog top extending into the lower temperature inversion layer but below the inversion top at all times. The lower inversion layer was between 50 m and 130 m in height, with a temperature at the top (bottom) of 6°C (2°C), changing later to 5.5°C (3°C), implying a weakening. On the other hand, the upper-level fog (as a component of the dual-layered fog event) had lower temperatures at its top due to cooling via long-wave radiation, with a strong inversion structure above the fog top. Thus, the upper- and bottom-level fog components were marked by intense temperature inversions over their tops. As shown by the profile of mixing ratio, there was a distinct humidity inversion layer under the tops of both components; above the tops, the mixing ratio decreased rapidly. From the profile of winds, the two components were characterized by wind increasing with height inside the fog layers, maximizing at, or above, the fog tops. This was followed by a swift drop at higher levels, i.e., a zone of low-level jets located at, or above, the tops, blowing in a northerly direction at 5 m s^{-1} at the strongest. Li et al. (1982) asserted that these jets are the results of multi-layered temperature inversions, and stated that when multi-level inversions of high enough intensity occur in the temperature field

and exist for some length of time, multi-layered wind maxima should emerge in the vicinity of the inversion top or somewhat higher. The lower-level jet between the fog layers prevents their connection.

After 1000 LST, when solar radiation was enhanced, air temperature and mixing ratio increased rapidity away from the surface, leading to the gradual dispersal of temperature and humidity inversions. As a result, the fog lifted progressively.

4.2 Evolution of the horizontal and vertical structure of the wind field

Two instruments were used to assess the wind field in the boundary layer, one being the tether-sonde system and the other being the acoustic Doppler radar. As it was limited to observing winds only at certain altitude, the tether-sonde remained at a constant 600 m above ground, while the acoustic radar detected only winds near a height of 500 m, retrieving a complete set of wind sampling every 15 minutes. The altitude resolution of the tether-sonde surpassed that of the radar profiler (1 m vs. 10 m). In what follows, we shall analyze and compare the two sets of winds to gain insight into the vertical structure before, during, and after the fog.
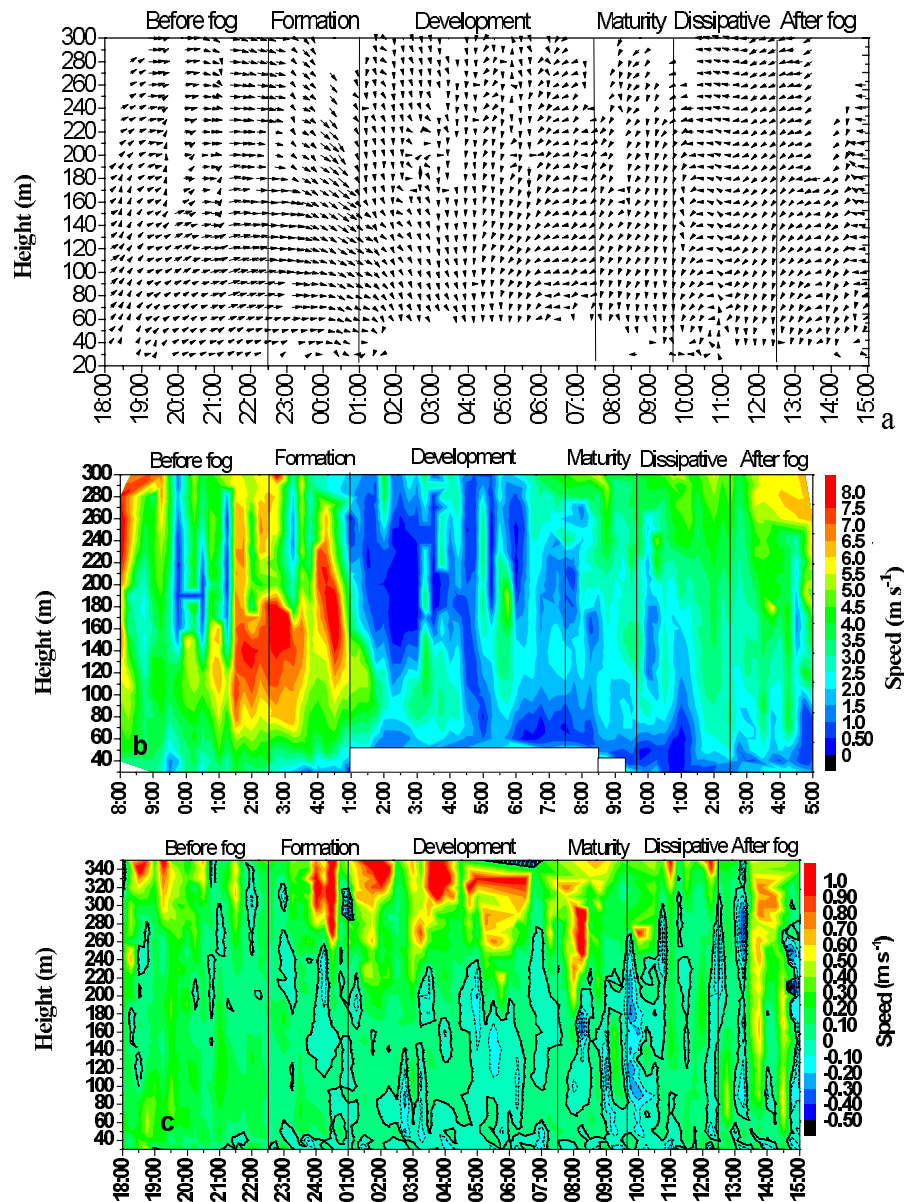
Fig. 4. Time-height section for horizontal and vertical winds detected by the acoustic Doppler radar from the pre-fog period until post-dispersal during 10–11 December 2007. (a) Wind direction (blank for invalid observations), (b) horizontal wind (gray denoting invalid soundings), and (c) vertical wind (positive values designating updrafts; negative and dashed lines representing downdrafts), with solid lines denoting zero values.

Figure 4 presents the time-height section of horizontal and vertical winds from pre-fog until dispersal as probed by the acoustic radar during 10–11 December 2007. Figure 5 delineates the height-evolving wind directions by means of the captive balloon, indicating that:

(1) In the pre-fog stage (prior to 2230 LST 10 December) the lower-level wind varied distinctly as a function of height, its direction turning clockwise with altitude (Fig. 4a) with the southwesterly wind in the near surface layer veering to westerly and later northwesterly flow as height increased, showing warm advection at low levels over Nanjing; winds below the 180-m level increased with time and altitude (Fig. 4b). Just prior to fog occurrence (2200–2230 LST) the 160-m level wind exceeded 7 m s^{-1} and the vertical wind was lower than 0.5 m s^{-1} (Fig. 4c).
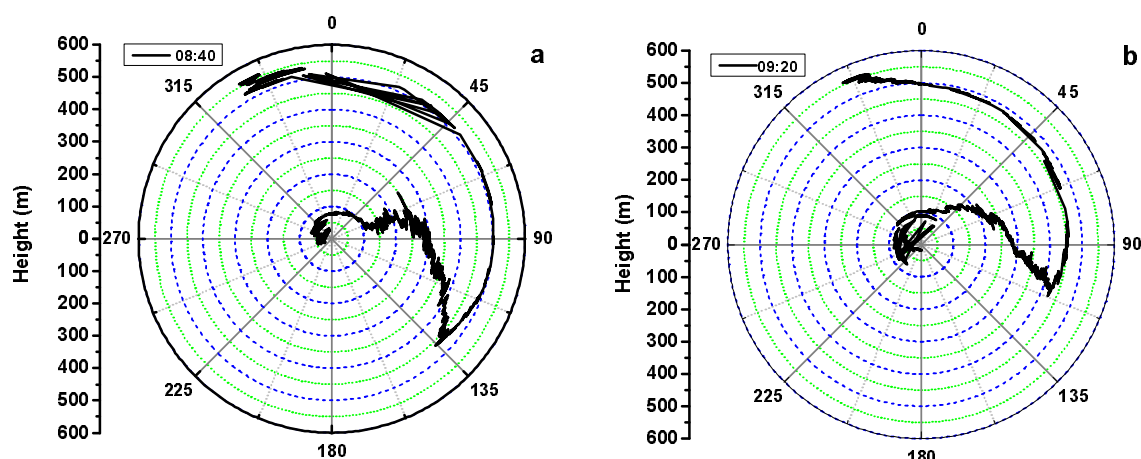
(2) During the formation stage (2230–0100 LST)

Fig. 5. Height-dependent wind on 11 December for the fog in its mature phase, with the *y*-axis denoting altitude and the coordinate-axis showing the wind direction. (a) 0840 LST; (b) 0920 LST.

stronger winds were found at 160 m, with weakening both above and below this zone. The surface wind dropped from 3 m s^{-1} before the fog to 1 m s^{-1} in the formation stage. The wind kept turning clockwise with height at all altitudes, so that westerlies occurred in the near-surface layer, and northwesterlies were present at low levels, with warm advection continuing to play a role in fog formation. In this stage, the vertical wind began to slowly weaken, approaching 0 m s^{-1}, and a brief period of very weak subsidence appeared near the surface. Around 0000 LST below and above the strong-wind zone at the 160 m level the wind shear increased, resulting in pronounced subsidence within the 100–240 m, stratum, contributing to the intensification of the subsidence inversion. The decrease in near-surface wind showed a gradual increase in atmospheric stability in favor of fog formation.

(3) In the development phase (0101–0730 LST) the wind turned clockwise with height as before, with weak winds observed throughout the low levels (<3 m s^{-1}; see Figs. 4a and 4b, where invalid soundings at below 50 m were removed), and surface wind was lower than 0.5 m s^{-1}. As the fog developed, the wind throughout the monitored area continued to turn clockwise, veering from northwest to north, and after 0500 LST the wind blew toward the northeast. Sinking air occurred below the 220 m level. Obviously, the reduced winds and the maintenance of the easterly wind and the subsidence allowed the thick fog to be sustained, contributing to circumstances allowing for the fog's explosive intensification.

(4) During the mature phase (0700–0940 LST), northerly wind dominated at lower levels, leading to a sharp drop in temperature. The surface fog experienced an explosive phase of development into an extremely dense fog (visibility <50 m). As depicted in

Figs. 5a and 5b, the wind veered clockwise with height through the 450 m level at first, followed by its turning counterclockwise with altitude, suggestive of cold advection capping the upper-layer fog, followed by the sinking of the cold advection air, causing the fog top to descend. Figures 5a and 5b also delineate that at 0840 LST, there was a zone of height-dependent counterclockwise-veering light winds from the 100- to 200- m level, indicative of weak cold advection, meaning that the vapor mixing ratio there was too low to give rise to fog formation (Fig. 3b). In addition, the vertical winds (Fig. 4c) showed that after the fog's explosive enhancement, from the near surface to the 200 m level rising air was present, which soon changed over to a downdraft in this stratum, while updrafts continued above the 240 m level. This indicates a disconnect between the upper- and lower-level fog components.

(5) In the dissipation phase (0940–1230 LST), the wind was changing in direction throughout the observed stratum, with the velocity intensifying gradually. Solar radiation became strong after sunrise and the vertical wind began to be directed progressively upward from the surface to the higher levels, with the fog being dispersed.

Based on the foregoing analysis, we conclude that during the surface fog formation, there was warm advection at lower levels, with light wind blowing over the ground and weak downdrafts in the near-surface layer. When the southeasterlies veered to northerly winds in this layer, the fog enhanced its explosive development, and there once existed rising air. A zone of low-level jets capped the fog zones from their tops, thus preventing the joining of the two separate fog layers. As air temperature began rising after sunrise, the horizontal wind began to strengthen and vertical wind was present throughout the observed area. At this

point, the surface fog started to disperse.

5. Disturbances of the boundary layer wind field

5.1 *Time-varying vertical distribution of low-level winds and of horizontal kinetic energy*

To investigate the effect of wind distribution in the boundary layer on dense fog formation, the acoustic Doppler radar data were utilized to explore wind variations, using the winds below the 500 m level.

Kinetic energy (KE) of air in a unit mass can be calculated via

$$\overline{\text{KE}} = \frac{1}{2}(\overline{u^2} + \overline{v^2}),\tag{1}$$

where the overbar indicates a time mean value; u and v are the zonal and meridional winds, respectively. Figure 6 presents the acoustic radar winds and the time-height mean KE obtained from Eg. (1), with the vertical lines α and β designating the start and end times of the fog, respectively. This analysis shows that:

(1) Prior to fog formation (1800–2000 LST 10 December), the mean KE was under 4 m^2 s^{-2} for the 40 m winds, suggestive of a stable atmosphere at this level, a condition favorable for radiative cooling in the near-surface layer. From the near-surface through the lower levels the KE of the winds increased rapidly, reaching 26 m^2 s^{-2} at the 180 m level when the fog formed, followed by a reduction afterward. Weakening winds are conducive to fog formation. When the fog was in the developing phase, the KE of the low-level winds substantially decreased, and so did the KE in the vertical, suggesting a stable stratification that contributed to the fog maintenance and development.

(2) The signals of KE disturbances at about 10 hours before the fog formation (see α vertical dashed lines in Fig. 6) revealed two maximum energy zones at 0400–0600 LST 10 December, one being in the near-surface layer and the other at the 100 m level. In both cases, the disturbances first increased and then decreased in intensity.

The disturbances increased again at both levels during 0800–1000 LST 10 December, and the maximum upper-level (100 m) disturbance spread to the 300 m level. After 1000 LST when the low-level KE decreased, the KE was stronger at the higher levels than at the middle levels (about 100–200 m), whose KE, in turn, exceeded that at the lower levels at 1200 LST (Fig. 6b). This time happened to be 10 hours ahead of the fog formation (2230 LST 10 December), a finding that is consistent with Zhang et al. (2005), who noted the same distribution of KE at the three
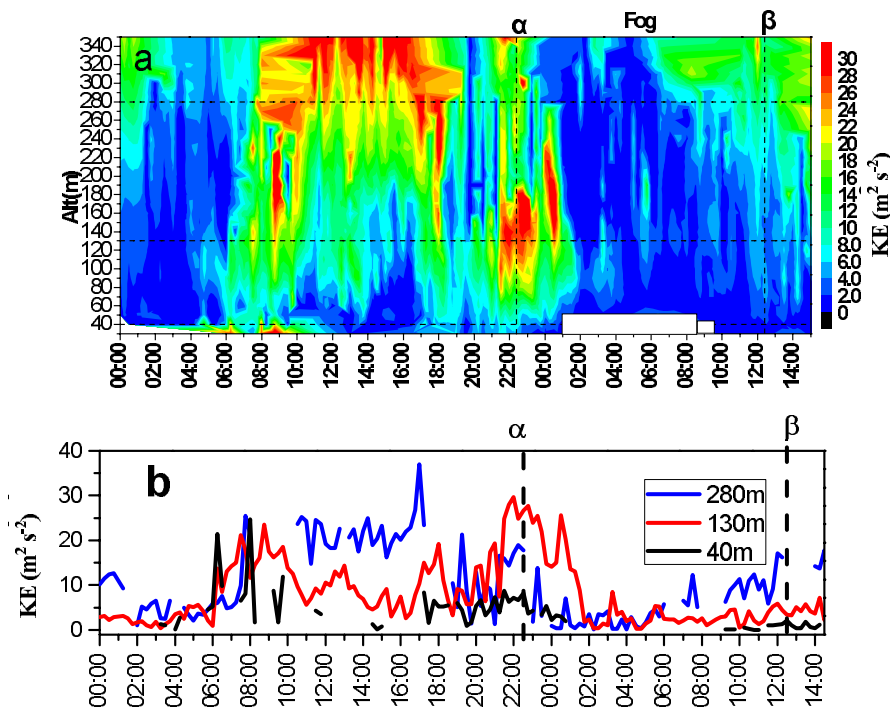

Fig. 6. Time–altitude section of (a) acoustic radar-obtained air kinetic energy during 10–11 December 2007 and (b) the kinetic energy for different heights (m), with the three altitudes shown in (b) corresponding to their counterparts (dotted lines) in (a). The vertical dashed lines at α and β refer to the start and end of the fog, respectively.

levels in their tower data. This key signal of the disturbance can be employed to predict fog formation.

Figure 6 depicts that the features of stronger KE at upper levels compared to middle and lower levels persisted from ~1200 to ~1800 LST 10 December; the fog was in its formation and development stages during the following 10 hours (2200 LST 10 December to 0400 LST on the following day). Over this time span there emerged multiple small "disturbances", each persisting for about one hour, and the KE was higher in the upper rather than the middle levels and was lowest at the lower levels. During the development phase, the visibility, LWC, and N of fog droplets experienced roughly 1 h disturbances (Figs. 1b and 1c).

5.2 *Variation in low-level turbulence*

The role played by turbulence in producing radiation fog is still unsettled. For example, some studies imply that stronger turbulence hinders the formation, and that so does very weak turbulence; others assert that turbulence may promote either the dispersal or intensification of fog (Welch, 1986; Zhou and Ferrier, 2008). Other studies (e.g., Gerber, 1981; Li et al., 1999; Nakanishi, 2000) note that increased turbulence is favorable for explosive growth due to broadening of the fog droplet spectrum. In the following section, ultrasonic anemometer data were used to investigate changes in turbulence during the course of the fog event.

Siebert and Teichmann (2000) assumed that there is no effect on the measurements of the subsidence of fog and water droplets in a fog event with regard to 3D wind measurements in a fog or cloud situation. To guarantee data quality, the following turbulence data were removed (Zhang et al., 2004), including (1) winds having an incidence angle of $> \pm 7°$ with the horizontal plane; (2) winds having a mean <0.2 m s^{-1}; (3) friction velocity <0.02 m s^{-1}; (4) sensible heat flux H_S <2 W m^{-2}; (5) other data for which the homogeneity of turbulence information was not ensurable.

An eddy correlation technique was used to process the turbulence data, and 1-minute mean data were employed to intensively analyze the variations of the turbulence in the near-surface layer.

The expressions for the related parameters are as follows:

(1) 3D perturbation wind speeds: $u' = u - \overline{u}$, $v' = v - \overline{v}$, $w' = w - \overline{w}$;

(2) standard deviation of wind speeds: $\sigma_u = \sqrt{\overline{u'u'}}$, $\sigma_v = \sqrt{\overline{v'v'}}$, $\sigma_w = \sqrt{\overline{w'w'}}$;

(3) horizontal wind speed: $U = (u^2 + v^2)^{1/2}$;

(4) turbulence intensities: $I_u = \sigma_u/U$, $I_v = \sigma_v/U$, $I_w = \sigma_w/U$;

(5) friction velocity: $u_* = \left[(-\overline{u'w'})^2 + (-\overline{v'w'})^2\right]^{1/4}$;

(6) normalized standard deviation of turbulence velocity (NSDTV): σ_u/u_*, σ_v/u_*, σ_w/u_* ;

(7) sensible heat flux: $H_S = \rho c_p \overline{\theta'w'}$ for the vertical transport of heat by turbulence, with positive (negative) value for upward and downward transport, respectively;

(8) mean turbulence KE (TKE): TKE$= (\overline{u'^2} + \overline{v'^2} + \overline{w'^2})/2$, where values denote vigor in direct relation to the transport of atmospheric momentum and heat as well as heat in the boundary layer, which also depends on atmospheric stability and solar radiation;

(9) vapor flux: $E = \rho\overline{q'w'}$;

(10) Monin-Obukhov length: $L = -u_*^3/(k\frac{g}{\theta}\overline{\theta'w'})$;

(11) stability parameter: Z/L, with $Z/L > 0$ for stable, $Z/L < 0$ for unstable, and $Z/L = 0$ for neutral states, where u, v, and, w are the instantaneous wind components; $\overline{u}$, $\overline{v}$, and $\overline{w}$, are the mean winds; ρ and $\theta(\theta')$ are the air density and potential temperature (turbulent part), respectively, obtained from synchronous measurements of pressure and temperature; $q(q')$ is the specific humidity (turbulent part), $k(=0.4)$ is the Karman constant; $g(=9.8$ m s$^{-2})$ is the gravitational acceleration; c_p is the specific heat at constant pressure; and Z is the height at which instrumental observations were made.

Figure 7 depicts the time-dependent change of the parameters listed above, indicating their variations during the formation and dissipation of the fog. Prior to formation (2230 LST 10 December), when the surface wind increased (from under 1 m s^{-1}), the turbulence intensity and its TKE increased, the friction velocity reached 0.3 m s^{-1}, the near-surface Z/L approached zero (weak instability), the vapor flux was almost constant, and the sensible heat flux was negative due to the radiative transfer of heat toward the surface. At this time the visibility dropped from 1500 m to less than 1000 m. It follows that very weak horizontal winds and appropriate turbulence intensities were responsible for the fog formation.

Following fog formation, wind speeds were reduced somewhat, leaving velocities on the order of 0.5 m s^{-1}, and the intensity of TKE and friction velocity were reduced in a wave-like manner, with diminishing NSDTV and the atmosphere tending toward neutral or weakly stable stratification. The latent heat released from fog droplets via condensation resulted in the sensible heat flux vanishing during this period, with visibility distance dropping from 1000 to 500 m. Thus, after fog formation the decrease in turbulence intensity and friction velocity was favorable for fog intensification.

Posterior to 0100 LST 11 December the fog was in the developing phase. In this phase the NSDTV
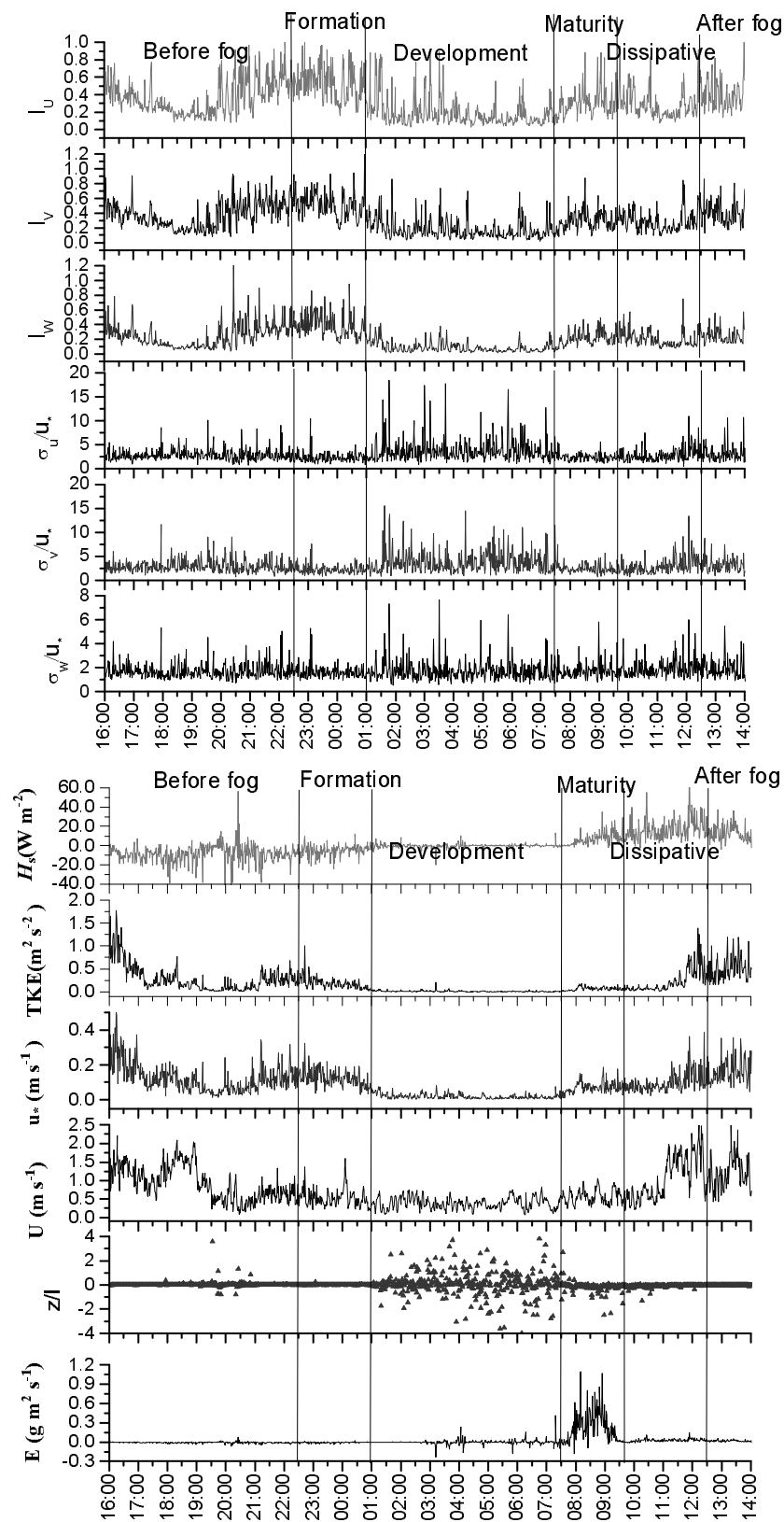
Fig. 7. Temporally-varying 1-min mean turbulence parameters at 3 m altitude during 10–11 December 2007 obtained at the observation site.
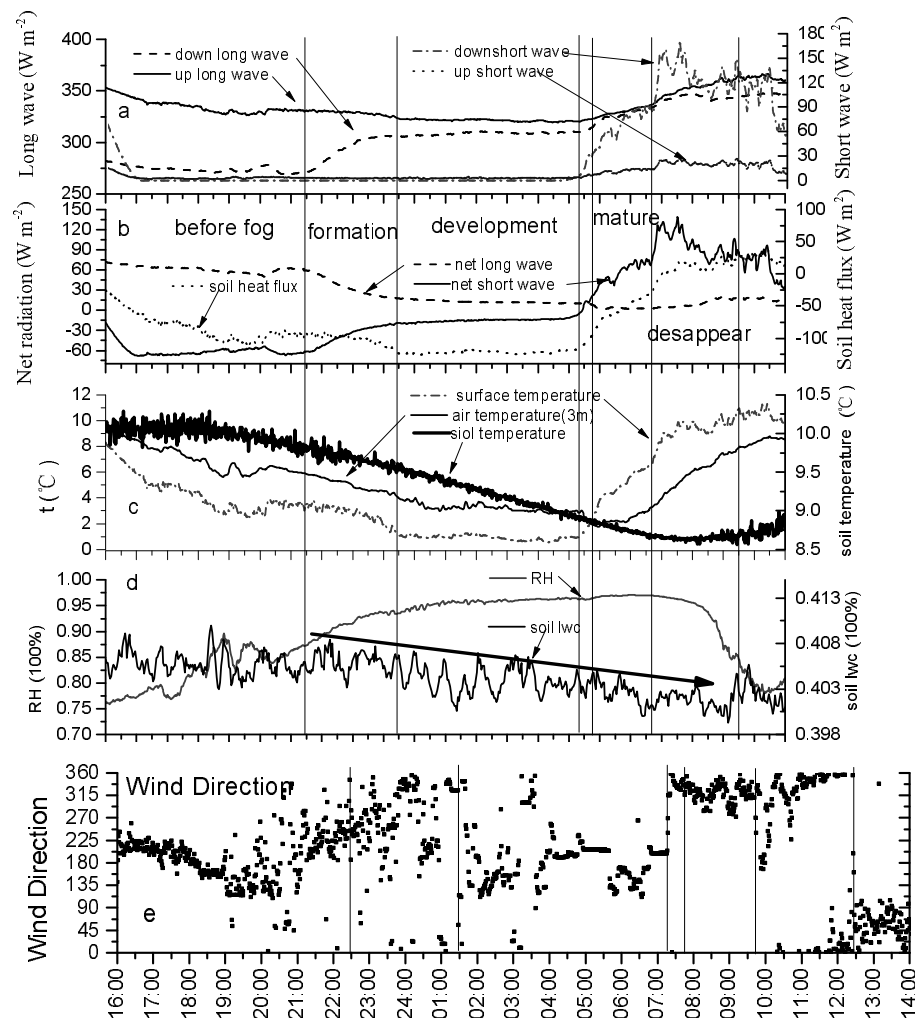
Fig. 8. Changes in radiation, temperature, and moisture in the near-surface layer and soil during 10–11 December related to the fog, with (a) scalar parameters, (b) positive values for downward net radiation, downward soil heat flux, and upward net long-wave radiation, (c) surface temperature, air temperature, and soil temperature, (d) RH in air and soil LWC, and (e) wind direction.

reached its maximum while the turbulence intensity (particularly I_w) and its mean TKE arrived at their minimum values, with diminishing sensible heat flux. The low-level atmospheric stratification (Z/L) varied between stable and unstable, with the microphysical structure varying greatly (Fig. 1).

After sunrise 0655 LST 11 December, when the low-level stratification varied between its stable and unstable states, the turbulence intensity and its TKE as well as the friction velocity began to increase, and the sensible heat flux became positive, enhancing itself progressively, while the vapor flux was augmented substantially. At 0720 LST, the wind veered from southeasterly to northerly, while the temperature dropped sharply (Fig. 8c) and the number density of droplets and the water content increased suddenly. As visibil-

ity decreased rapidly to less than 50 m, the explosive development of this fog further accelerated in the near-surface layer.

The distinct features after the extremely dense fog's appearance were as follows: the largest vapor flux was observed during the observation period, and sensible heat flux in excess of 0.0 and increasing successively was observed, along with significantly enhanced turbulence intensity and the stratification changing alternately from stable to unstable. As the temperature rose, the turbulence intensity weakened and then intensified, with unstable stratification remaining at the lower levels. Wind speed, as well as the turbulent wind speeds and TKE, intensified greatly compared to the minimum of the vapor flux. In this stage, the fog dispersed gradually.

Based on the foregoing analysis, we conclude that both fog formation and its reinforced explosive development occurred when turbulence intensity and friction velocity were noticeably increased. The vapor flux was maximal in extremely dense fog phase. In the mature stage, the turbulence intensity became weaker, and when vapor flux dropped to its minimum levels the fog began to dissipate.

6. Variation in radiation flux and air-surface exchanges of heat and vapor

The radiation fog started when strong surface cooling occurred. In a clear nighttime sky, breezes, high relative humidity, and stable atmospheric stratification contribute to fog formation and development. In the process of surface cooling, the upward soil heat flux and vapor flux play an immensely important role in fog formation, development, and maintenance. The role of the air-surface transfers of radiation energy, heat, and moisture is discussed next.

Starting during the pre-fog period at 1600 LST 10 December, when outgoing long-wave radiation was stronger compared to incoming long-wave radiation (see Fig. 8a), surface temperature dropped quickly from 8°C at 1600 LST to 2.4°C at 2100 LST (Fig. 8c). Correspondingly, the net long-wave radiation was reduced from 70 to 51 W m^{-2} (Fig. 8b). As the surface was cooled, the air provided radiant energy directly to the colder surface (see augmented downward sensible heat shown in Fig. 7), leading to readings of 9.1°C at 1600 LST to 5.7°C at 2100 LST for the 3 m air temperature (Fig. 8c). The cooler surface allowed heat to be fluxed upward from the soil (Fig. 8b), and soil heat flux increased from 30 to 107 W m^{-2} (1600 vs. 2100 LST), which was responsible for the drop in soil temperature (Fig. 8c). As the soil thermal flux arrived at the surface, this compensated for the heat loss via surface radiation, causing a further surface-temperature drop (see 2100 LST in Fig. 8c). The soil-temperature drop occurred synchronously with reduced water content (Fig. 8d). This was because the soil-driven flux, while transporting heat upward also carried vapor in the same direction. When air temperature dropped and moisture increased, relative humidity in the air began to gradually be enhanced (Fig. 8d) so that the visibility dropped to less than 1000 m at 2230 LST as fog formed. In that period, the wind veered from southwesterly to westerly, with the velocity declining progressively to 0.5 m s^{-1}.

Subsequent to fog formation, the downward long-wave radiation in the fog increased and surface net long-wave radiation weakened progressively as the fog deepened and its concentration increased. The sur-face and 3 m temperature and continued to decline; soil temperature dropped due to augmented soil heat flux, and soil moisture was decreasing, as well.

In the phase of fog development, the upward and downward long-wave radiation intensities were kept nearly constant (321 compared to 308 W m^{-2}), with little change of temperature at the surface and the 3 m level (0.7°C–0.9°C vs. 2.8°C–3.5°C). The soil provided the surface with a thermal flux of 118–125 W m^{-2}, leading its temperature to drop slowly (the surface temperature was maintained at the cost of upward soil thermal flux). The soil water content declined because of steady transport of vapor to the surface. As a result, net long-wave radiation was kept constant, indicating that the fog's depth was unchanged and so was its intensity. From the surface to the lower levels there was a temperature gradient, with temperature increasing as a function of height, and the stable inversion structure favored the steady development of the fog.

After sunrise (0655 LST) the surface net radiation increased, and so did the surface-absorbed net short-wave radiation flux which rose more sharply, leading to an appreciable rise in surface temperature. However, air temperature in the near-surface layer did not increase but rather decreased rapidly. This was due to the fact that part of the rain water remaining at the surface from the day before began to evaporate, resulting in augmented vapor flux as the evaporation consumed heat (Fig. 7). From 0722–0730 LST 11 December, the wind veered from southeasterly to northerly (Fig. 8), and increased in velocity. The cold advection also decreased temperatures. As seen in Fig. 8, the temperature dropped 0.5°C in 8 min. Surface water evaporation and the rapid decrease of temperature permitted the air to be saturated, leading to intensified explosiveness, with visibility reduced from 120 m to 15 m.

The surface temperature at 0740 LST was the same as the 3-m temperature, leading to the disappearance of the inversion layer below the 3 m level. This caused an unstable near-surface stratification that evolved from lower to higher levels after sunrise, resulting in enhanced turbulence that permitted fog droplets to coalesce and the fog layer to grow upward.

From the foregoing analysis, we conclude that weak cold advection, fast-dropping temperatures, plentiful vapor supply, and increased turbulence gave rise to the droplet growth via condensation and increased coalescence, broadening the spectrum of droplets so that the fog developed with augmented explosiveness into an extremely dense fog in a short time.

The mature phase of the fog followed its explosive development. In this period, solar radiation heated the

surface, leading surface and near-surface temperatures to rise quickly and also leading to enhanced long-wave radiative flux and reduced soil heat flux. The temperature profile in Fig. 3 shows that the inversion layer was lifted nearly to the height of the fog top. In the meantime, the soil water content continued to decrease, and LWC reduced slowly in the near-surface layer. The number density of droplets in the small size classes declined and MDD was maintained above 30 μm, thereby illustrating that in this stage droplets began to evaporate and the downward long-wave radiation gradually approached the sane magnitude as the outgoing radiation owing to the deepening of the dual-layer fog (Fig. 3).

With enhanced solar radiation, surface temperature increased gradually and turbulent diffusion transported heat into the air, causing temperature to rise in the near-surface layer and the fog to disappear, a situation responsible for the evaporative dispersal of droplets in the near-surface layer. In addition, the gradient of low-level wind began to increase (Fig. 3), augmenting the wind shear at the fog top, dragging drier air into the fog layers and thus dispersing it. When the fog was about to dissipate, soil heat content started to decline below the surface and soil moisture began to increase.

7. Concluding remarks

Our conclusions are as follows:

(1) The case described herein is a typical radiation fog event. Strong radiative cooling occurred first, followed by air immediately above the surface losing heat to the cooled area above, causing cooling there. Meanwhile, soil-evaporated moisture increased the relative humidity in the air, resulting in fog droplets.

(2) Inspection of continuous observations of fog microphysical structure and visibility demonstrate that this extremely dense radiation fog event was separable into four phases: formation, development, mature, and dissipation. The water content and number density of droplets varied greatly from phase to phase, with the maximum water content reaching 0.47 g m^{-3} and the largest number density topping out at 798 cm^{-3} during the mature stage. These values are orders of magnitude higher (4 orders and 2 orders, respectively) compared to those in the formation phase.

(3) The development of the dense fog (visibility distance <500 m) into an extremely dense fog (visibility distance <50 m) took 20 minutes, with water content increasing explosively by 3 orders of magnitude and MDD by threefold. These changes were related to the increased evaporation from the surface and the invasion of weak cold air after sunrise.

(4) The extremely dense fog was dual-layered, with the fog-level tops capped by intense inversions of temperature and humidity. The low-level jets between the two fog layers prevented them from joining.

(5) The fog took place in a region of stable stratification when the turbulence intensity and its TKE as well as friction velocity were appreciably elevated. These changes all dissipated swiftly after the fog occurrence, leading to a neutral or weakly stratified state. In the development stage, these factors were at their minima, allowing the atmospheric stratification to vary between stable and unstable states. When these variables increased again, the fog was in the process of explosive development, with low-level stratification changing to an unstable state. In the dissipation phase, although the turbulence weakened, the stratification was unstable, so the sensible heat flux was augmented appreciably.

(6) The mean KE before fog formation was rather weak, and afterwards it increased quickly from the surface to low levels, maximizing below 200 m when the fog formed. The low-level KE in both the horizontal and vertical directions decreased markedly in the development and mature stages.

REFERENCES

Ahn, M. H., E. H. Sohn, and B. J. Hwang, 2003: A new algorithm for sea fog/stratus detection using GMS-5 IR data. *Adv. Atmos. Sci.,* **20**, 899–913.

Bergot, T., and D. Guedalia, 1994: Numercial forecasting of radiation fog. Part I: Numerical model and sensitivity tests. *Mon. Wea. Rev.*, **122**, 1218–1230.

Bott, A., U. Sievers, and W. Zdunkowski, 1990: A radiation fog model with a detailed treatment of the interaction between radiative transfer and fog microphysics. *J. Atmos. Sci.*, **47**, 2153–2166.

Cao, X. C., R. Jie, M. Y. Zhou, S. M. Li, and N. P. Lü., 1998: Artificial fog dispersal and variation of atmospheric boundary layer properties in Beijing Capital Airport. *Acta Geophysica*, **41**, 773–779. (in Chinese)

China Meteorological Administration (CMA), 2003: *Meteorological Surface Observational Norms.* China Meteorological Press, Beijing, 151pp. (in Chinese)

Duynkerke, P. G., 1991: Radiation fog: A comparison of model simulation with detailed observations. *Mon.*

Wea. Rev., **119**, 324–341.

Fuzzi, S., and Coauthors, 1992: The Po valley fog experiment in 1989. *Tellus*, **44**, 448–468.

Gao, S. H., H. Lin, B. Shen, and G. Fu, 2007: A heavy sea fog event over the Yellow Sea in March 2005: Analysis and numerical modeling. *Adv. Atmos. Sci.,* **24**, 65–81, doi: 10.1007/s00376-007-0065-2.

Gerbert, H. E. 1981: Microstructure of radiation fog. *J. Atmos. Sci.*, **38**, 454–458.

Gultepe, I., and Coauthors, 2007: Fog research: A review of past achievements and future perspectives. *Pure Appl. Geophys.*, **164**, 1121–1159.

Gultepe, I., and Coauthors, 2009: The fog remote sensing and modeling field project. *Bull. Amer. Meteor. Soc.*, **90**, 341–359.

Huang, J. P., Q. Y. Mei, Y. C. Jin, and Z. H. Li., 1998a: Microphysical structure Features and Evolution processes of radiation fog in Huning Rigion. *Meteorological Monthly*, **24**, 3–8. (in Chinese)

Huang, J. P., S. W. Zhu, and B. Zhu, 1998b: Characteristics of the atmospheric boundary layer during radiation fog. *Journal of Nanjing Institute of Meteorology,* **21**, 258–265. (in Chinese)

Huang, J. P., Z. H. Li, Y. R. Huang, and Y. S. Huang, 2000: A three-dimensional model study of complex terrain fog. *Chinese J. Atmos. Sci.*, **24**, 821–834. (in Chinese)

Huang, Y. S., W. R. Xu, Z. H. Li, L.Fan, and W. J. Huang, 1992: An observation and analysis on the radiation fog in Xishuangbanna. *Acta Meteorologica Sinica*, **50,** 112–117. (in Chinese)

Li, Z. H., J. P. Huang, B. Y. Sun, and H. Peng, 1999: Burst characteristics during the development of radiation fog. *Chinese J. Atmos. Sci.*, **23**, 623–631. (in Chinese)

Li, X. S., C. J. Zhu, L. Q. Liu, A. Y. Zheng, and M. Y. Zhou, 1982: A study on multi-level wind velocity profile in the planetary boundary layer. *Chinese J. Atmos. Sci.*, **6**, 308–314. (in Chinese)

Liu, D. Y., M. J. Pu, J. Yang, G. Z. Zhang, W. L. Yan, and Z.H. Li, 2010: Microphysical structure and evolution of a four-day persistent fog event in Nanjing in December 2006. *Acta Meteorologica Sinica*, **24**, 104–115.

Nakanishi, M., 2000: Large-eddy simulation of radiation fog. *Bound. Layer Meteor.*, **94**, 461–493.

Nishikawa, T., S. Maruyama, and S. Sakai, 2004: Radiative heat transfer and hydrostatic stability in nocturnal fog. *Bound.-Layer Meteor.*, **113**, 273–286.

Niu, S. J., C. S. Lu, H. Y. Yu, L. J. Zhao, and J. J. Lü, 2010: Fog research in China: an overview. *Adv. Atmos. Sci.*, **27**, 639–662, doi: 10.1007/s00376-009-8174-8.

Pu, M. J., G. Z Zhang, W. L.Yan, and Z. H. Li, 2008a: Features of a rare advection–radiation fog event. *Science in China* (D), **38**, 776–783.

Pu, M. J., W. L. Yan, Z. T. Shang, J. Yang, and Z. H. Li, 2008b: Study on the physical characteristics of burst reinforcement during the winter fog of Nanjing. *Plateau Meteorology*, **27**, 1–8. (in Chinese)

Siebert, H., and U. Teichmann, 2000: Behavior of an ultrasonic anemometer under cloudy conditions. *Bound. Layer Meteor.*, **94**, 165–169.

Taylor, G. I., 1917: The formation of fog and mist. *Quart. J. Roy. Meteor. Soc.*, **43**, 241–268.

Welch, R. M., M. G. Ravichandran, S. K. Cox, 1986: Prediction of quasi-periodic oscillations in radiation fogs. Part I: Comparison of simple similarity approaches. *J. Atmos. Sci.*, **43**, 633–651.

Yin, Q., and S. Z. Xu, 1994: A numerical study on the formation and dissipation of radiation fog (II): The physical mechanism of radiation fog. *Acta Meteorologica Sinica*, **52**, 60–67. (in Chinese)

Zeng, X. M., and P. Q. Huang, 1998: A numerical model of advection-radiation fog within shallow-water swamp-land area. *Climatic and Environmental Research*, **3**, 266–293. (in Chinese)

Zhang, G. Z., L. G. Bian, J. Z. Wang, Y. Q. Yang, W. Q. Yao, and X. D. Xu., 2005: The boundary-layer characteristics in the heavy fog formation process over Beijing and its adjacent areas. *Science in China* (D), **48**(Suppl.2), 88–101.

Zhang, H. S., F. Y. Li, and J. Y. Chen, 2004: Statistical characteristics of atmospheric turbulence in different underlying surface conditions. *Plateau Meteor*ology, **23**, 598–604. (in Chinese)

Zhang, L. M., and Z. H. Li, 1993: A two-dimensional time-integral numerical model of Chongqing fog. *Chinese J. Atmos. Sci.* **17**, 750–775. (in Chinese)

Zhou, B. B., and B. S. Ferrier, 2008: Asymptotic analysis of equilibrium in radiation fog. *Journal of Applied Meteorology and Climatology*, **47**, 1704–1722.